

Unfolding the mechanism of the AAA+ unfoldase VAT by a combined cryo-EM, solution NMR study

Rui Huang^{a,b,c,1}, Zev A. Ripstein^{c,d,1}, Rafal Augustyniak^{a,b,c}, Michal Lazniewski^{e,f}, Krzysztof Ginalski^e, Lewis E. Kay^{a,b,c,d,2}, and John L. Rubinstein^{c,d,g,2}

^aDepartment of Molecular Genetics, University of Toronto, Toronto, ON, Canada M5S 1A8; ^bDepartment of Chemistry, University of Toronto, Toronto, ON, Canada M5S 3H6; ^cDepartment of Biochemistry, University of Toronto, Toronto, ON, Canada M5S 1A8; ^dThe Hospital for Sick Children Research Institute, Toronto, ON, Canada M5G 0A4; ^eLaboratory of Bioinformatics and Systems Biology, Centre of New Technologies, University of Warsaw, 02-089 Warsaw, Poland; ^fDepartment of Physical Chemistry, Faculty of Pharmacy, Medical University of Warsaw, 02-097 Warsaw, Poland; and ^gDepartment of Medical Biophysics, University of Toronto, Toronto, ON, Canada M5G 1L7

Edited by Gerhard Wagner, Harvard Medical School, Boston, MA, and approved June 1, 2016 (received for review March 9, 2016)

The AAA+ (ATPases associated with a variety of cellular activities) enzymes play critical roles in a variety of homeostatic processes in all kingdoms of life. Valosin-containing protein-like ATPase of *Thermoplasma acidophilum* (VAT), the archaeal homolog of the ubiquitous AAA+ protein Cdc48/p97, functions in concert with the 20S proteasome by unfolding substrates and passing them on for degradation. Here, we present electron cryomicroscopy (cryo-EM) maps showing that VAT undergoes large conformational rearrangements during its ATP hydrolysis cycle that differ dramatically from the conformational states observed for Cdc48/p97. We validate key features of the model with biochemical and solution methyl-transverse relaxation optimized spectroscopy (TROSY) NMR experiments and suggest a mechanism for coupling the energy of nucleotide hydrolysis to substrate unfolding. These findings illustrate the unique complementarity between cryo-EM and solution NMR for studies of molecular machines, showing that the structural properties of VAT, as well as the population distributions of conformers, are similar in the frozen specimens used for cryo-EM and in the solution phase where NMR spectra are recorded.

VAT | proteasome | protein dynamics | cryo-EM | methyl-TROSY NMR

The AAA+ enzymes (ATPases associated with a variety of cellular activities) use the energy of ATP hydrolysis to carry out a myriad of different biological functions that are critical to cellular homeostasis. These molecular machines are typically barrel-shaped, containing a narrow channel that serves to traffic substrates through the enzyme (1–4). In the case of the heat shock protein 104 (Hsp104) AAA+ class of chaperone, for example, substrates are dissociated from aggregates via a pulling motion that forces individual polypeptide chains through the central pore of the enzyme (1, 5). The unfolded proteins that emerge subsequently refold spontaneously or are acted on by additional chaperones that aid in their refolding (6). Other AAA+ enzymes act synergistically with proteases, unfolding targeted substrates and passing them directly to the proteases, where they are subsequently degraded (7). In this way, proteins that have become damaged or that are no longer required can be removed before their accumulation disrupts cellular function (8). A variety of different AAA+ unfoldases have been characterized, including Rpt1–6 in the 19S proteasome regulatory particle in eukaryotes (9–11), PAN in archaea (12–14), Mpa/ARC in Actinobacteria (15), ClpA/X (2) and HslU (3) in bacteria, and VAT in the *Thermoplasma acidophilum* archaeobacterium (16–20).

VAT is an ~500-kDa homohexamer, with each monomer containing two tandem AAA+ domains, referred to as D1 and D2, and an N-terminal domain (NTD) distinct from the NTD of other AAA+ enzymes (16) (Fig. 14). Both D1 and D2 are homologous to the single AAA+ modules of PAN and Rpt1–6 (1, 16). Biochemical studies have shown that VAT unfolds globular proteins and interacts directly with the 20S core particle (CP) of the proteasome, leading to enhanced proteolytic activity for both folded and unfolded protein substrates (18–21). In eukaryotes,

the enzymes Cdc48 and p97/VCP, which are homologous to VAT, play essential roles in a large number of cellular functions, including transcriptional and metabolic regulation, cell cycle progression, membrane fusion, apoptosis, and protein degradation (22). Interestingly, eukaryotic analogs of VAT, such as Cdc48 and p97, lack critical Tyr residues in the pore loops of the D1 domain that are important for unfolding protein substrates and passing them into the lumen of the enzyme. However, substitution of the native residues with Tyr and removal of the NTD in mouse Cdc48 lead to a mutant enzyme that can unfold protein substrates and collaborate with both mouse and archaeal 20S CPs in protein degradation (20, 23).

The ATP hydrolysis activity required for the function of VAT and other AAA+ unfoldases leads to conformational changes in AAA+ ring structures that vary from local rearrangements of secondary structure to large-scale domain motions (1, 7, 24–26). However, the mechanism by which many of these proteins carry out their function remains to be elucidated. The inherent flexibility of these complexes, coupled with the important role of what are likely to be large-scale dynamics during the unfoldase cycle, can complicate structural analyses of the unfolding reaction by

Significance

Cellular function is tightly regulated by large molecular assemblies such as the proteasome, which is involved in the removal of damaged or misfolded proteins. Proteasome substrates are unfolded by complexes such as valosin-containing protein-like ATPase of *Thermoplasma acidophilum* (VAT) via a process that is coupled to ATP hydrolysis. We used a combined electron cryomicroscopy (cryo-EM) and NMR analysis to show that VAT undergoes large, previously unidentified, conformational changes that are essential for substrate unfolding and to suggest a model by which the energy released upon ATP hydrolysis can be coupled to the unfolding process. Our approach demonstrates that cryo-EM/NMR studies offer the exciting potential of obtaining both structural and dynamic information that, together, can provide a detailed understanding of how molecular machines function.

Author contributions: R.H., L.E.K., and J.L.R. designed research; R.H., Z.A.R., and L.E.K. performed research; R.A., M.L., and K.G. contributed new reagents/analytic tools; R.H., Z.A.R., and L.E.K. analyzed data; R.H. and L.E.K. wrote the paper; R.H. and L.E.K. initiated the project; R.H. and Z.A.R. prepared figures; and J.L.R. supervised the electron cryomicroscopy studies.

The authors declare no conflict of interest.

This article is a PNAS Direct Submission.

Data deposition: All electron cryomicroscopy maps described in this article have been deposited in the Electron Microscopy Data Bank (EMDB) (accession nos. EMD-3435 and EMD-3436).

¹R.H. and Z.A.R. contributed equally to this work.

²To whom correspondence may be addressed. Email: kay@pound.med.utoronto.ca or john.rubinstein@utoronto.ca.

This article contains supporting information online at www.pnas.org/lookup/suppl/doi:10.1073/pnas.1603980113/-DCSupplemental.

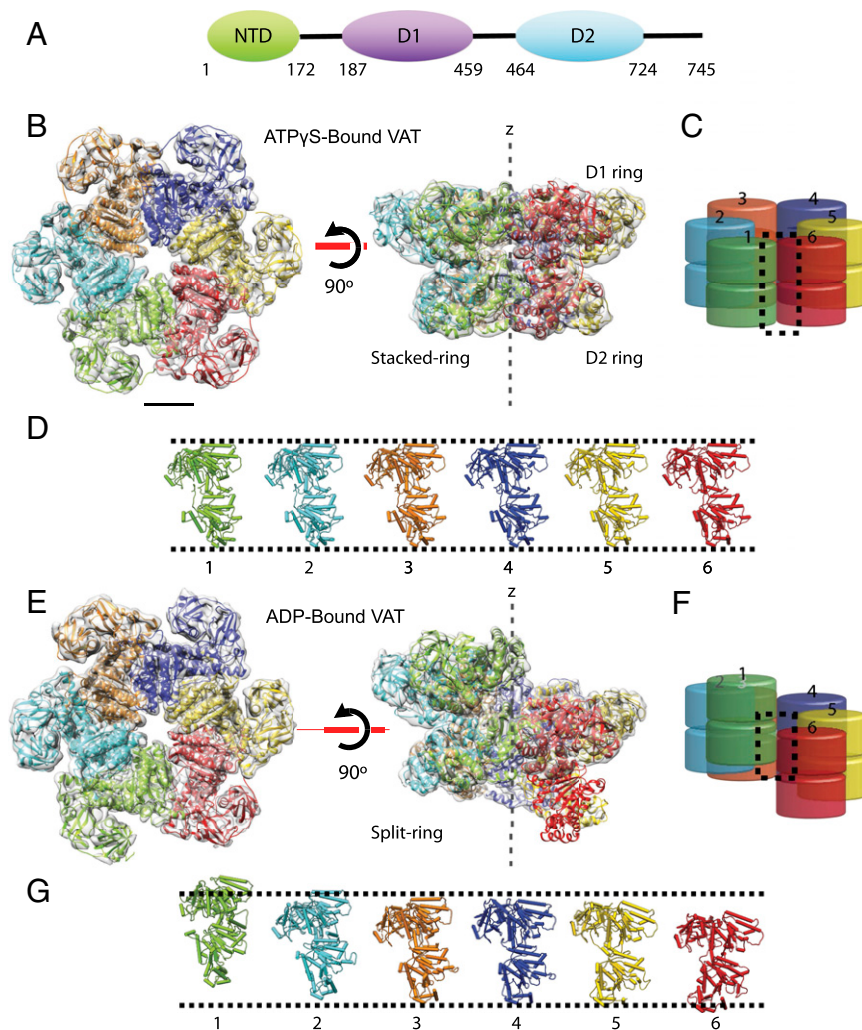


Fig. 1. VAT can assume different conformational states depending on the bound nucleotide. (A) VAT is composed of three domains, including an NTD (green) and a pair of AAA+ nucleotide binding domains, D1 (purple) and D2 (blue) (16). Domain boundaries are indicated via the numbers in the figure. (B) Cryo-EM density maps and a fitted atomic model for the stacked-ring, ATP γ S-bound form of VAT showing the prototypical coaxial ring arrangement of the D1 and D2 hexameric rings. Each of the protomers is color-coded. (C) Schematic of the stacked-ring VAT structure, highlighting the D1/D1 and D2/D2 interfaces between adjacent protomers by means of the dashed rectangle. Note that although a majority of ATP γ S VAT structures are stacked, a sizable fraction also assumes the split-ring structure that is the only conformer formed in the ADP-loaded state. (D) Unwinding the stacked-ring conformation in C with each protomer shown in the same orientation. Note that each protomer has been rotated, but the relative position along the z axis is preserved. (E) Cryo-EM-derived structure of ADP-VAT, showing the helical arrangement of the six protomers. Although the density of D2 of protomer 6, in particular, is weak, a complete protomer atomic model has been fitted in the map. (F) Schematic highlighting the unique interface between protomers 1 and 6 (dashed rectangle) whereby D1/NTD of protomer 6 contacts D2 of protomer 1, which leaves D2 of protomer 6 and D1 of protomer 1 without all of their interacting partners. (G) Unwinding the splitting conformation in E with each protomer shown in the same orientation. (Scale bar, 25 Å.)

X-ray crystallography. In this context, the emergence of other biophysical methods, such as electron cryomicroscopy (cryo-EM) (27, 28) and solution NMR spectroscopy (NMR) (29, 30), offers unique possibilities to examine both the structure and the dynamics of AAA+ machines such as VAT, the focus of this report.

The introduction of direct detector device (DDD) cameras for electron microscopes has dramatically improved the signal-to-noise ratio in cryo-EM images, allowing calculation of 3D maps that resolve protein secondary structure, and even side-chain detail in many cases, for proteins as small as 150 kDa (31). Perhaps equally important, the enhanced signal from DDDs allows effective sorting of populations of single-particle images into classes corresponding to different 3D structures, enabling the identification of different conformations of molecules that exist simultaneously in the specimen (32, 33). However, how the populations of these different 3D classes from ice-embedded specimens relate to conformer populations existing in solution remains unclear.

Studies of biomolecules by solution NMR have traditionally been limited to systems with aggregate molecular masses on the order of 50 kDa or less. However, the development of new NMR experiments that protect against rapid signal decay using the transverse relaxation optimized spectroscopy (TROSY) principle (34, 35) along with labeling approaches that can be optimally exploited by the TROSY approach (36), coupled with hardware improvements such as cryogenically cooled probes, has significantly reduced the size barriers that were once so limiting. It is thus possible to obtain detailed, site-specific, structural and dynamical

information on molecular complexes in the 1-MDa size range (37). In this regard, combined cryo-EM/NMR studies offer the exciting potential of obtaining both high-resolution structures (from cryo-EM) and dynamics (from NMR) that, together, can lead to a more complete understanding of function than what could be obtained from either method in isolation.

With this synergy in mind, we present a structural and biochemical investigation of the VAT AAA+ unfoldase using a combined cryo-EM/solution NMR approach. Analysis of the cryo-EM data establishes distinct conformations for the hexameric VAT ring in ATP γ S- and ADP-loaded states, suggesting a large-scale domain rearrangement during cycles of nucleotide binding and hydrolysis. In the ADP-loaded state, VAT protomers are arranged in a helical manner, resulting in a split-ring conformation. In contrast, when loaded with ATP γ S, VAT adopts both the split-ring structure and a conformation whereby pairs of rings comprising the six D1 and six D2 domains stack collinearly, with the sixfold symmetry axis running through the central pore of the complex. The structures elucidated by cryo-EM are validated through biochemical and NMR studies. Notably, reasonable agreement was obtained between cryo-EM and NMR analyses of the relative populations of split- and stacked-ring conformations, especially considering that the cryo-EM specimen was prepared by rapid freezing of a solution from 4 °C, whereas the NMR studies were performed at 60 °C. This level of agreement demonstrates that the rapid freezing used in cryo-EM studies faithfully preserved equilibrium solution populations and that 3D classification can measure

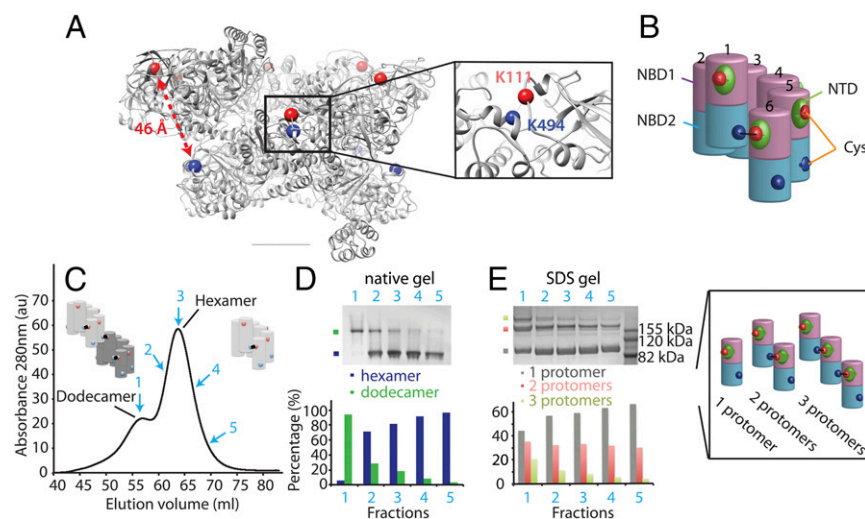


Fig. 2. Biochemical experiments support the split-ring ADP-VAT structure. (A) Cryo-EM structure of ADP-VAT highlighting positions 111 and 494 in red and blue, respectively, which have been mutated to cysteine. (B) Of the 12 cysteines that are introduced into a cysteine-free version of VAT, only 1 pair, C111 from the NTD of protomer 6 and C494 of protomer 1, are close enough to form a disulfide bond, as illustrated schematically. (C) SEC profile of cross-linked ADP-VAT. au, arbitrary units. (D) Percentage of dodecamers, resulting from interhexamer disulfide bonds, and hexamers can be resolved using native gel electrophoresis under nonreducing conditions, showing that fraction 5 is very highly enriched in hexamers (>95%). Shown along the y axis is the percentage of the total protomers that are in hexamer and dodecamer complexes. (E) SDS/PAGE of SEC fractions 1–5 (nonreducing conditions), which resolves individual and cross-linked protomers. Shown along the y axis is the percentage of total protomers that are in one-protomer, two-protomer (one cross-link), and three-protomer (two cross-links) species. The approximate 65%:35% ratio (fraction 5) for one- and two-protomer (i.e., singly cross-linked) species is as predicted for hexameric VAT with a single interprotomer cross-link.

these populations accurately. Finally, a series of ATP hydrolysis and substrate unfolding studies using a cross-linked version of VAT that is locked into the split-ring conformation establishes the importance of the split-/stacked-ring conformational interconversion for optimal VAT function. In addition to providing insights into the structure and function of VAT, the present work illustrates the unique complementarity between cryo-EM and solution NMR in studies of molecular machines.

Results

Cryo-EM Structures of ADP- and ATP_γS-Bound VAT Complexes Show Distinct Conformations. We used single-particle cryo-EM to obtain structural models of the hexameric AAA+ protein VAT in both ADP- and ATP_γS-loaded states. For the ADP-loaded state, 912 micrographs were collected and subjected to automatic particle selection, 2D classification, and 3D classification, with no symmetry applied. This analysis yielded a single asymmetrical 3D class containing 71,258 particle images that was refined to 7.0-Å resolution, sufficient to resolve α -helices clearly (Figs. S1 and S2). The map shows VAT in a split-ring conformation that has not been observed previously for p97/VCP (38–42). For the ATP_γS-loaded state, 514 micrographs were collected and subjected to a similar analysis. However, for this state, two distinct 3D classes were detected: one that resembled the split-ring conformation seen for the ADP-loaded state and an additional stacked-ring conformation that appeared sixfold symmetrical, reminiscent of crystal structures and EM maps of p97/VCP (38–42) (Fig. S3). The asymmetrical split-ring map from the ATP_γS-loaded state was refined to 12-Å resolution with 7,539 particle images, whereas the stacked-ring map was refined to 7.8-Å resolution with 16,538 particle images and the application of C6 symmetry (Fig. 1 B–D and Fig. S1). Alignment in three dimensions and Fourier shell correlation (criterion of 0.5) of the split-ring conformations from the ADP- and ATP_γS-loaded states of VAT show the maps to be identical up to the 12-Å resolution limit of the map of this conformation from the ATP_γS-loaded state (Fig. S4); consequently, we consider the split-ring conformation from the two different enzyme preparations to be equivalent. To date, there is no atomic

resolution structure of VAT. However, an atomic model is available for a mammalian homolog, mouse p97 (39–42), which has ~45% sequence identity with the *T. acidophilum* VAT. Thus, a homology model was built for VAT using the crystal structure of mouse p97 [Protein Data Bank (PDB) ID code 3CF3] and the NMR structure of VAT NTD (PDB ID code 1CZ4). The D1, D2, and NTD domains of the model were fit independently into the corresponding cryo-EM density maps and subsequently refined by molecular dynamics flexible fitting (43).

In the sixfold symmetrical, stacked-ring conformation of VAT (Fig. 1 B and C), the D1 and D2 rings are both planar and align on top of each other coaxially, with the NTDs packed against the periphery of the D1 ring in a coplanar fashion. Unwinding the protomer arrangement shown in Fig. 1C produces the “structural snap-shots” illustrated in Fig. 1D. Notably, the “tops” and “bottoms” of each protomer align, as expected, due to the symmetry of the model.

Upon ADP binding, VAT adopts a split-ring conformation as indicated in Fig. 1E and in the schematic of Fig. 1F. The arrangement of protomers is helical, with each successive protomer descending along the z axis of the map (Fig. 1F), and we have chosen to label the protomers from 1 to 6 as indicated in Fig. 1. However, the split-ring helix has a variable pitch with larger steps along the z axis from protomer 1 to 2 and from protomer 5 to 6 than between other adjacent protomers. This unequal spacing can be seen in Fig. 1G, where the protomers of the split-ring structure have been unwound to produce snap-shots that show the relative differences in translation along the z axis.

The structures of the six individual protomers in the split-ring conformation can be superimposed well, but the relative orientations of the D1 and D2 domains differ slightly in each protomer, with a variance of ~1.2°. Notably, the progressive descent of protomers along the z axis leads to a substantial offset between protomers 1 and 6, forming an atypical interface between them (compare dashed boxes in Fig. 1 C and F). In the case of the split-ring structure, D2 of protomer 1 is in direct contact with NTD/D1 of protomer 6. In this conformation NTD/D1 of protomer 1 and D2 of protomer 6 lack contacts with neighboring

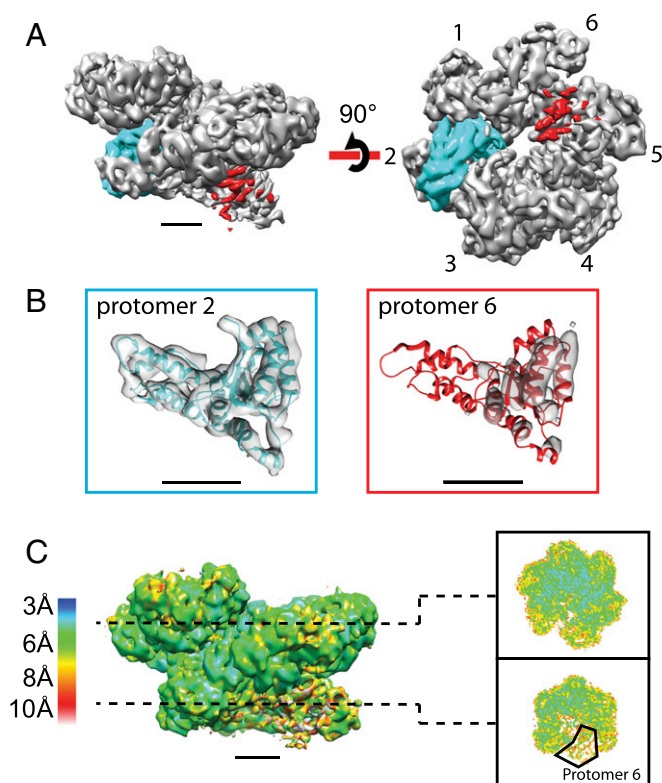


Fig. 3. Protomer 6 is poorly defined in cryo-EM density maps of ADP-VAT. (A) Density map of ADP-VAT highlighting the D2 domains of protomers 2 (blue) and 6 (red). (Scale bar, 25 Å.) (B) Comparison of segmented density for the D2 domains of protomers 2 and 6. A large portion of the D2 domain from protomer 6 shows fragmented density due to inherent flexibility. (Scale bar, 25 Å.) (C) Local resolution estimation for the split-ring conformer shows that the flexible D2 domain of protomer 6 is at a lower resolution than the rest of the map. A pair of horizontal slices through regions corresponding to D1 (Top) and D2 (Bottom) emphasizes the lack of structural definition for D2 of protomer 6.

protomers that are present at the other protomer–protomer interfaces. Close inspection of the protomer 1–protomer 2 interface establishes that the contacts formed between D1 and D2 are similar to the D1/D1 and D2/D2 contacts at the other interfaces, reflecting the high degree of sequence similarity between the D1 and D2 domains.

A comparison of the split- and stacked-ring conformers suggests that large-scale domain movements accompany the nucleotide hydrolysis cycle in VAT. In addition to the apparent movements in the positions of the protomers along the *z* axis that accompany the split/stacked-ring interconversion, as can be seen in a comparison of Fig. 1 *B–D* and *E–G*, each protomer undergoes relative rotations of the D1 and D2 domains by $\sim 14^\circ$ (Fig. S5 and Movie S1). The rotation of each protomer suggests a cooperative mechanism by which the pivoting of each subunit around the D1–D2 linker accompanies the large-scale rearrangement of the hexamer from a stacked-ring conformation to a split-ring conformation or vice versa.

Intramolecular Cross-Linking Validates the ADP Split-Ring Conformation.

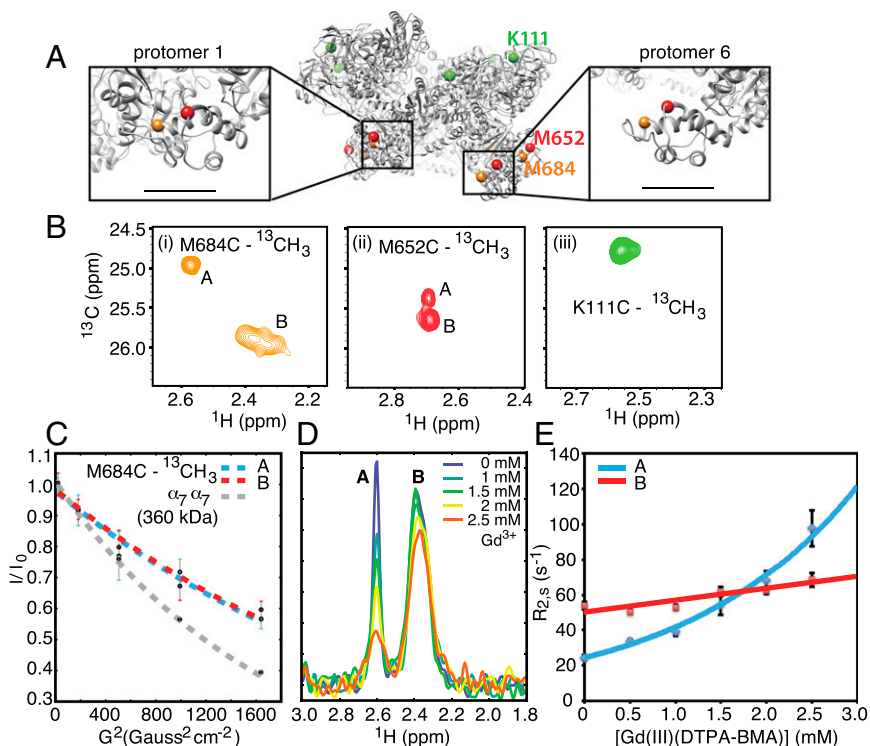
As described above, ADP-bound VAT was observed to exist exclusively in a split-ring conformation, whereas both split- and stacked-ring structures were obtained for the ATP γ S-loaded complex. To establish that the split-ring conformation of ADP-VAT is not an artifact of the freezing process and is populated in solution, we performed cross-linking studies. Here, a cysteine-free construct of VAT (C77A/C679A) was used, into which a pair of cysteines, K111C (localized to the NTD) and K494C

(on D2), was introduced in each protomer via mutagenesis. Positions 111 and 494 were chosen based on the cryo-EM model of ADP-VAT, which shows that among the 12 cysteines introduced into each VAT hexamer in this manner, only two are sufficiently close to each other for disulfide bond formation (C^β within 8 Å), with all other pairs more than 43 Å apart (Fig. 2A). We would thus predict on the basis of the cryo-EM model that a single intramolecular disulfide bond would be formed between the two cysteines at the interface between protomers 1 and 6, as depicted by the black line in Fig. 2B.

Copper-1,10-phenanthroline was used as an oxidizing catalyst to promote disulfide bond formation (44). The solvent accessibility of the added cysteines can result in intermolecular cross-linking, leading to dodecamers or higher order oligomers of ADP-VAT, as depicted in Fig. 2C (Left Inset). Therefore, we first characterized the oxidation product by size exclusion chromatography (SEC). Higher order oligomers of VAT that result from inter-VAT cross-linking could be distinguished and separated from hexameric VAT by SEC (Fig. 2C). Different fractions in the SEC elution profile were subjected to further analysis by native gel electrophoresis. The native gel resolves dodecameric and hexameric VAT complexes (Fig. 2D, Upper), from which the percentage of each species in each fraction could be quantified (Fig. 2D, Lower). Consistent with their respective elution volumes, the VAT compositions of fractions 1–5 show a transition from the dodecameric species (fraction 1) to the hexameric species (fraction 5), with an inversion in the relative amounts of each species from fraction 1 to fraction 5. Further insight into the population distribution of cross-linked protomers was obtained from SDS/PAGE, where one protomer (86 kDa), two linked protomers (172 kDa), and three linked protomers (258 kDa) were observed (Fig. 2E). Approximately 45% of the total number of protomers are found as the one-protomer species in SEC fraction 1, which increases to $\sim 65\%$ in fraction 5. The amount of the two-protomer species remains constant throughout the SEC fractions, but the amount of the three-protomer species decreases significantly from fraction 1 to fraction 5. Because the three-protomer species can only result from formation of dodecamers or higher order oligomers, the decreasing number of the three-protomer species in SDS/PAGE with increasing fraction number (Fig. 2E, light green) mirrors the decrease in the percentage of dodecamers in the corresponding fractions in the native gel (Fig. 2D, green). Notably, in fraction 5, which is predominantly composed of hexameric VAT ($>95\%$; Fig. 2D), the number of protomers in cross-linked two-protomer and single-protomer species has an approximate ratio of 1:2 (Fig. 2E). This result is consistent with an intramolecular disulfide bond connecting two of the six protomers (33%) in a VAT molecule, as indicated schematically in Fig. 2B and predicted on the basis of the cryo-EM split-ring model of ADP-VAT.

Once the asymmetrically cross-linked hexamer was isolated, an excess of maleimide was added to “cap” cysteine residues at the remaining 111 and 494 positions to prevent formation of dodecamers or higher order structures, as described in *SI Materials and Methods*. The oxidation product of fraction 5 was further subjected to digestion with trypsin, followed by mass spectrometry characterization, confirming the existence of protein fragments cross-linked by residues 111 and 494. As a final test, we carried out cryo-EM analysis of cross-linked C111–C494 ATP-VAT. In contrast to wild-type (wt) ATP γ S-bound VAT, where both split- and stacked-ring conformations were observed, formation of the disulfide bond led exclusively to the split-ring structure (Fig. S6). Taken together, the structural and biochemical data demonstrate the spatial proximity of K111 and K494 at a single-protomer interface of VAT in the ADP-loaded state and provide strong evidence in support of the split-ring model.

Fig. 4. Solution NMR results are consistent with structural heterogeneity in ADP-VAT. (A) Three sites were chosen for placement of methyl group probes, position 111 in the NTD (green) and positions 652 (red) and 684 (orange) in D2, highlighted on the split-ring structure of ADP-VAT. Mutations were made to produce K111C, M652C, and M684C, to which was added ^{13}C -MMTS to generate an S-methylthio-cysteine residue. (Insets) Zoomed-in regions containing residues 652 and 684, illustrating the difference in chemical environments of the methyl probes in a "typical" protomer, protomer 1 (Left) and the "atypical" protomer 6 (Right). Note that only a single site (111, 652, or 684) is labeled with an S-methylthio-cysteine residue in each NMR sample (corresponding to six probes per hexamer). (B) ^{13}C - ^1H methyl TROSY spectra of S-methylthio-cysteine probes at positions 684 (i), 652 (ii), and 111 (iii) of ADP-VAT. A pair of peaks, which we label as A and B, are observed in spectra recorded on samples labeled at positions 684 and 652. (C) Identical diffusion constants quantified from peaks A and B are obtained from pulsed-field gradient diffusion measurements. The intensity ratios of NMR peaks in a 2D ^{13}C - ^1H correlation map (I/I_0 , where I and I_0 are peak intensities in the presence and absence of the gradient G , respectively) are plotted as a function of the square of the labeling gradient (G^2). Shown also is the decay of magnetization from the half-proteasome, $\alpha_7\alpha_7$, as a function of G^2 . The decay curves are given by the relation $I = I_0 \exp(-ADG^2)$, where D is the translational diffusion constant and A is a constant that depends on experimental parameters that were identical in each of the reported measurements. (D) Peak intensities in spectra of M684C- $^{13}\text{CH}_3$ VAT vs. concentration of added paramagnet, plotted as a series of ^1H projections from 2D ^{13}C - ^1H datasets. (E) Slow component of methyl ^1H R_{2s} rate as a function of added paramagnet.



Structural and Dynamic Heterogeneity in the Split-Ring VAT Conformation. The arrangement of protomers forming the splitting helical conformation shown in Fig. 1 *E–G* results in different protomer–protomer interfaces along the z axis. The interface between protomers 1 and 6 is distinct from the other protomer–protomer interfaces, shown schematically in Fig. 1*F* (using the same numbering scheme as above), where the interface is formed between NTD/D1 of protomer 6 and D2 of protomer 1. In contrast, the other protomer interfaces are stabilized by contacts involving D1/D1 and D2/D2 interactions between domains of neighboring protomers. The lack of interprotomer contacts involving D2 of protomer 6 at the interface between protomers 1 and 6 leads to structural heterogeneity, as can be seen clearly in the cryo-EM maps. Fig. 3 *A* and *B* highlights D2 domains of protomers 2 (blue) and 6 (red) in the context of the full structure (*A*) and for the extracted domains (*B*), clearly illustrating that the relative density for the D2 subunit of protomer 6 is lower than for the other protomers, suggesting conformational heterogeneity. Fig. 3*C* shows a map of local resolution (45) in the split-ring conformation, and includes a pair of slices through the resolution map for regions corresponding to the D1 (*Top*) and D2 (*Bottom*) domains, which emphasizes the limited resolution in the map for D2 of protomer 6.

To explore the structural and dynamic heterogeneity within VAT further, we used solution-based NMR techniques that are optimized for studies of high-molecular-weight complexes. Typical applications make use of $^{13}\text{CH}_3$ labeling of Ile, Leu, Met, and Val methyl groups in an otherwise highly deuterated background, in concert with methyl-TROSY-based experiments that exploit the labeling scheme (30, 37). Although labeling methyl groups from a variety of amino acids increases the number of probes of structure and dynamics, a drawback is that cross-peaks in spectra must first be assigned to specific residues in the primary sequence, and the assignment process can be a major bottleneck in applications involving a 500-kDa complex with

protomer subunits approaching 100 kDa in molecular mass. We therefore made use of an alternative strategy whereby methyl groups are added to key positions that directly report on structural and/or dynamic features of interest. This specificity is achieved through the use of ^{13}C -methyl-methanethiosulfonate (^{13}C -MMTS), which labels cysteine side chains with $^{13}\text{CH}_3$ -S to form S-methylthio-cysteine (46). To this end, we introduced a single cysteine mutation into cysteine-free VAT (C77A/C679A) at three positions (111, 652, and 684; one per sample) followed by attachment of $^{13}\text{CH}_3$ groups to the highly deuterated protein, using a procedure described previously (46). Fig. 4*A* shows that residues 111, 652, and 684 localize to the NTD (111, green) and D2 (652, red and 684, orange) domains of VAT.

Unlike what would be expected for a symmetrical hexamer, we observed two cross-peaks for $^{13}\text{CH}_3$ groups attached to positions 684 (Fig. 4*B*, *i*) and 652 (Fig. 4*B*, *ii*) in methyl-TROSY ^{13}C - ^1H -correlated NMR spectra (35) of ADP-loaded VAT, suggesting two distinct local environments for these methyl probes. The cross-peaks do not originate from a heterogeneous population of VAT molecules composed of intact and proteolyzed complexes, for example, because diffusion constants obtained from pulse-field gradient NMR measurements (47) quantifying each peak separately are statistically identical: 2.7 ± 0.3 and $2.6 \pm 0.3 \times 10^{-7} \text{ cm}^2 \text{ s}^{-1}$ for peaks A and B, respectively (Fig. 4*C*, blue and red; 40 °C). Notably, the diffusion of the VAT complex is slower than for the half-proteasome (30) control, $\alpha_7\alpha_7$ ($4.6 \pm 0.3 \times 10^{-7} \text{ cm}^2 \text{ s}^{-1}$), as expected on the basis of the lower molecular mass of the $\alpha_7\alpha_7$ complex (360 kDa vs. 500 kDa; Fig. 4*C*, gray).

A clue as to the identities of peaks A and B is obtained from their fractional areas (quantified by peak integration) of $28 \pm 2\%$ and $72 \pm 4\%$, respectively, as measured in spectra with the label at D2 position 684 (Fig. 4*B*, *i*) or 652 (Fig. 4*B*, *ii*). Skewed areas would be expected if peaks A and B originate from methyl spin probes localized to protomer 6 and potentially protomer 5 (peak A), and to protomers 1–4 (peak B), with a ratio approximately

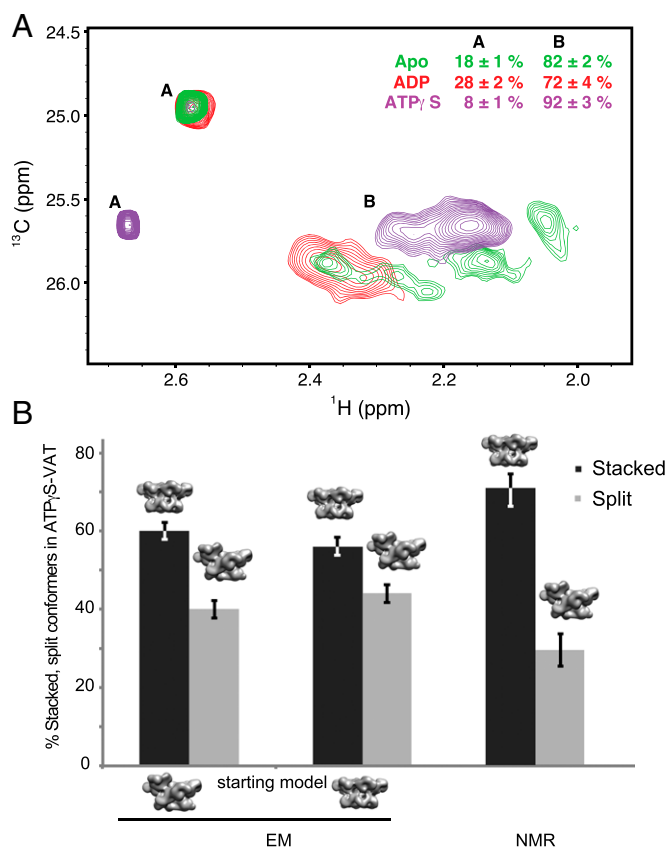


Fig. 5. Nucleotide binding shifts the relative populations of stacked- and split-ring conformers. (A) Methyl-TROSY spectra of $^{13}\text{CH}_3$ -labeled S-methylthio-cysteine attached at position 684 to apo-VAT (green), ADP-VAT (red), and ATP γ S-VAT (purple). Fractional intensities of each of the cross-peaks [A/(A + B), B/(A + B)] are indicated in the upper right corner. (B) Comparison of the fractional populations of stacked- and split-ring structures for ATP γ S-VAT obtained by cryo-EM and NMR methods.

the same as observed experimentally. Moreover, that pairs of peaks are observed is consistent with the cryo-EM model of the split-ring conformation that establishes distinct arrangements of the D2 domains for protomers 1–4 vs. protomer 6, and thus different magnetic environments for the attached methyl probes. For example, the methyl probe in protomer 6 is localized to a region of low density in the EM map, whereas the corresponding probe in protomer 5 faces D2 of “structurally heterogeneous” protomer 6. Thus, probes in protomers 5 and 6 could well have identical chemical shifts (peak A), with similar shifts for the remaining methyls in protomers 1–4 (peak B). If this assignment is correct, a prediction would be that placement of an S-methylthio-cysteine residue in a position that is much less “heterogeneous” across the protomers would give rise to a single peak in NMR spectra. We therefore recorded spectra with a methyl probe localized to position 111 in the complex (Fig. 4A, green), and only a single peak was observed (Fig. 4B, iii).

To support this assignment further, we carried out paramagnetic relaxation NMR experiments by adding a soluble spin label, Gd(III)DTPA-BMA (48), that leads to a decrease in the signal intensity from an NMR active probe by an amount related to its surface accessibility, and hence exposure to the paramagnet. Fig. 4D shows the intensity change of peaks in spectra of M684C- $^{13}\text{CH}_3$ ADP-VAT, plotted as a series of ^1H projections from 2D ^{13}C - ^1H datasets, as a function of added paramagnet. Notably, peak A decreases much more rapidly than peak B. We also measured methyl ^1H transverse relaxation ($R_{2,s}$) rates (49)

(Fig. 4E); because the rate is biexponential for a methyl group attached to a protein (35), we selected the slowly relaxing component of magnetization (49). As expected, $R_{2,s}$ rates increase much more rapidly as a function of Gd(III)DTPA-BMA concentration for peak A than for peak B. This observation, together with the faster decrease in intensity for the peak A resonance, indicates that peak A derives from probes localized to regions with higher solvent accessibilities than for peak B. In this regard, it is noteworthy that solvent accessibilities for positions 684 and 652, as calculated from the split-ring VAT model, are significantly higher for protomer 6 than for protomers 1–4, especially for position 684, where the surface accessibility is ~90% for protomer 6, relative to 20–30% for protomers 1–4. Note that we have chosen not to report surface accessibilities for residues 652 and 684 of protomer 5 because the region of D2 containing these residues faces protomer 6, which is not well defined, and any calculation of accessibility that does not take into account the dynamics of protomer 6 would not be meaningful. The ^1H $R_{2,s}$ rate measured for peak A of M684C- $^{13}\text{CH}_3$ ADP-VAT in the absence of Gd(III)DTPA-BMA ($24.5 \pm 1.3 \text{ s}^{-1}$) is significantly smaller than the value for peak B ($53.8 \pm 2.0 \text{ s}^{-1}$) (Fig. 4E; [Gd(III)DTPA-BMA] = 0), suggesting higher flexibility for the S-methylthio-cysteine probe in protomer 6 relative to the other protomers, as expected on the basis of the high surface accessibility calculated from the cryo-EM map. The increased mobility of the probe localized to protomer 6 was further confirmed by recording an F₁-scalar-coupled ^1H - ^{13}C heteronuclear single quantum coherence (HSQC) dataset of M684C- $^{13}\text{CH}_3$ ADP-VAT (Fig. S7). For a highly dynamic methyl group, and neglecting relaxation, a 3:1:1:3 quartet structure is expected in such a spectrum (50). In contrast, for methyls attached to slowly tumbling macromolecules, the outer lines decay approximately ninefold faster than the inner components (51, 52), so that for rigid methyl groups, the outer lines often disappear (35). It is clear that the outer lines are significantly more pronounced for peak A than for peak B, indicating increased dynamics at this site (protomer 6).

Having established that peaks A and B provide direct probes of the different D2 domains of protomers 1–6, we were interested in measuring the rate of protomer interconversion (i.e., exchange between protomer states giving rise to peaks A and B). To this end, magnetization exchange experiments (53) were recorded; notably, cross-peaks connecting the two states were not observed. Calculations establish an upper bound for the exchange rate, $k_{ex} = k_{AB} + k_{BA}$, on the order of 0.2 s^{-1} for the $A \xrightleftharpoons[k_{BA}]{k_{AB}} B$ process (Fig. S8), where A and B denote the protomer states giving rise to peaks A and B, respectively. Such a slow rate might be expected on the basis of the large activation barrier that no doubt must be overcome in the interconversion between two conformers with significantly different structures.

Shifts in VAT Conformational Landscape with Different Nucleotides.

We recorded methyl-TROSY spectra of $^{13}\text{CH}_3$ -labeled S-methylthio-cysteine attached to position 684 in the apo (Fig. 5A, green), ADP-loaded (Fig. 5A, red), and ATP γ S-loaded (Fig. 5A, purple) states. We also attempted to study adenylyl-imidodiphosphate (AMP-PNP)-loaded VAT; however, the sample was not stable and precipitated above 40 °C. In analogy to the ADP-bound form, protomer states A and B could be assigned for both the ATP γ S and apo forms of the complex, with the methyl probe in state A clearly more dynamic than probes in state B. As with ADP-VAT, there appears to be increased conformational heterogeneity in state B for ATP γ S- and apo-VAT, especially for the apo form of the enzyme, where multiple dispersed peaks are observed. Notably, it was only possible to obtain a cryo-EM map at ~30-Å resolution from 16,585 particle images for nucleotide-free VAT, consistent with the structural heterogeneity observed by NMR. It is worth noting that the significant change in the position of peak A in the ATP γ S state is likely due to the nucleotide

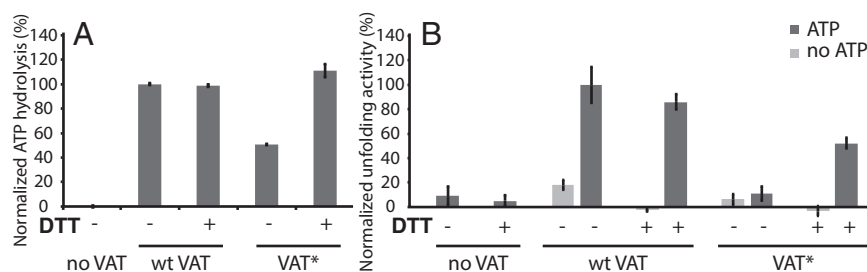


Fig. 6. Interconversion between stacked- and split-ring structures is critical for efficient function of VAT. (A) Normalized ATPase activity of wt VAT and of a VAT double mutant (K111C/K494C) cross-linked once per complex at the protomer 1–6 interface (VAT*), in the absence (–) or presence (+) of DTT. (B) Unfoldase activity of VAT toward the substrate GFP11 under both oxidizing (–DTT) and reducing (+DTT) conditions, and in the presence (black) or absence (gray) of ATP, following the procedure of Horwich and coworkers (56).

because the position of the probe is proximal to the nucleotide binding pocket.

We quantified the relative intensities of cross-peaks A and B for the nucleotide-bound and nucleotide-free forms of VAT as indicated in Fig. 5A, which can be directly related to populations of the split- and stacked-ring structures. Significant differences in intensities were observed for the different nucleotide states, indicating that the relative abundance of split- and stacked-ring conformers can be controlled through the binding of nucleotides. Assuming that only the split-ring conformer is present in the ADP-loaded state in solution, as is suggested by our cryo-EM analysis, we calculated fractional populations of $28 \pm 4\%$ and $72 \pm 4\%$ for split- and stacked-ring structures in the ATP γ S-bound form of VAT in solution (Fig. 5B, Right) from the populations of the A/B protomer states.

We also estimated the populations of the two different conformations of the ATP γ S-loaded VAT complex by comparison of the number of particle images in each class after 3D classification (Fig. 5B, Left and Center). To determine the systematic error of this method, we divided the data into three random nonoverlapping subsets that were analyzed separately. The 3D maximum likelihood classification algorithm that we used (54, 55) requires an initial 3D reference to begin the classification. To control for bias introduced by this reference, we performed the 3D classification with a low-pass-filtered (to 40 Å) split-ring map as the starting reference (Fig. 5B, Left) and a low-pass-filtered stacked-ring map as the starting reference (Fig. 5B, Center). The populations of the split-ring ($42 \pm 3\%$) and stacked-ring ($58 \pm 3\%$) conformations estimated by cryo-EM (Fig. 5B, Left and Center) show the same trend as the population estimate from NMR (Fig. 5B, Right). Furthermore, a paired Student's *t* test was performed to determine if any bias had been introduced from the starting model to the calculation of populations, but no significant difference was observed between runs with different starting models.

Interconversion Between Split- and Stacked-Ring Conformers Is Essential for Optimal Function. Our cryo-EM results establish that VAT undergoes a large conformational change between split- and stacked-ring structures. How might this change be related to function? To address this question, we returned to the K111C/K494C VAT double mutant that is cross-linked once per complex (Fig. 2 C–E; fraction 5), so that the enzyme is locked in the split-ring conformation [Fig. 2B; subsequently referred to as cross-linked VAT (VAT*)]. Unfolding activities of VAT* under both oxidizing and reducing conditions were measured and compared with the unfolding activities of wt VAT. Locking the enzyme in the split-ring conformation (Fig. 6A; VAT* – DTT) leads to an approximate 50% decrease in ATPase activity compared with wt VAT, which can be recovered upon disulfide bond reduction (Fig. 6A; VAT* + DTT). The unfolding activity of VAT was assayed by measuring the rate of decrease of fluorescence of GFP11 that

accompanies unfolding. To ensure that the unfolded GFP11 cannot refold, we used an assay developed by Horwich and coworkers (56) whereby unfolded GFP11 is captured by a D87K mutant of GroEL that prevents substrate release. In this manner, we found that the unfolding activity of locked VAT* is almost abolished (Fig. 6B; VAT* – DTT), because similar rates of unfolding are obtained relative to a control that lacks VAT or ATP (Fig. 6B; no VAT or no ATP). Reduction of the disulfide bond leads to ~50% recovery of the net unfolding activity compared with wt. The lack of complete recovery of unfoldase activity may be a function of the added cysteines at positions 111 and 494 (12 residues) in combination with maleimide capping of the remaining 10 cysteines so as to prevent formation of higher order structures. The results of this assay establish the importance of the large split-/stacked-ring conformational rearrangement for VAT function.

Discussion

Recent advances in cryo-EM, including the development of DDD cameras, coupled with image classification algorithms, have greatly facilitated high-resolution structure determination of biomolecular machines (27, 28). Because it is possible to elucidate structures of different conformers that exist in a specimen, cryo-EM offers the possibility of obtaining insight into how conformational changes may be linked to function. However, cryo-EM experiments involve trapping conformations by rapid freezing and subsequent quantification of populations with classification algorithms. How accurately these estimates of population distributions mirror the populations in solution had not been studied previously. Solution NMR spectroscopy has also developed to the point where atomic resolution studies of molecular machines are possible (57) through improved instrumentation, novel labeling, and spin physics methodologies. NMR has emerged as a powerful tool to characterize different functional states of biomolecules in solution, even in cases where the states are sparsely populated and only transiently formed (58). As such, both cryo-EM and solution NMR are complementary, and a combination of both methods holds great promise for studies of heterogeneous, dynamic systems.

Here, we used cryo-EM to produce models of the AAA+ protein VAT in both ADP- and ATP γ S-bound states. Notably, an asymmetrical conformation was observed for the ADP-loaded state in which the six VAT protomers are arranged as a helix with variable pitch, leading to differences in interprotomer interfaces along the helical axis. The difference is especially pronounced for the first and last protomers in the helix, denoted by 1 and 6 in Fig. 1 E–G and Fig. 2B, where D1–D2 interactions are formed rather than the “canonical” D1/D1 and D2/D2 contacts observed in crystal structures and cryo-EM maps of p97 (38–42) and manifest in the split-ring arrangement seen for VAT. The result is that the D2 domain of protomer 6, in particular, lacks many of the interactions that are present in other D2 domains, and its

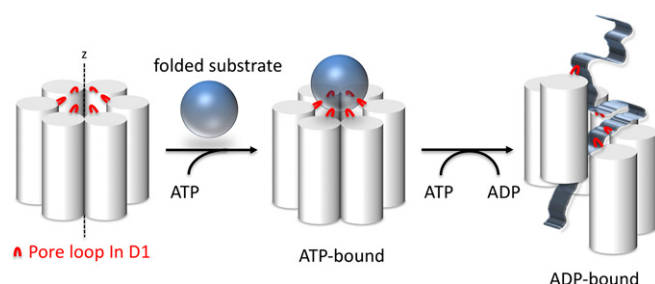


Fig. 7. Proposed mechanism for VAT function. (Left) Schematic of the ATP-VAT structure showing the sixfold symmetrical arrangement of the protomers and the position of the D1 pore loop residues (red) at the top of the structure. Binding of folded substrate (blue) occurs initially via the pore loops (Center), with subsequent ATP hydrolysis generating the force required for substrate unfolding and threading through the axial pore (Right).

density is notably weak (Fig. 3). This low density in the map is most likely due to flexibility of this region, which results from the lack of stabilizing contacts with a neighboring D2 domain. In contrast to ADP-loaded VAT, where only a single conformer is observed, both split- and stacked-ring structures are present in EM specimens of ATP γ S-VAT. The stacked-ring conformation positions the D1 and D2 hexameric rings on top of each other, forming a cylindrical structure (Figs. 1 B–D). The large structural changes between stacked- and split-ring conformers described above are also accompanied by rotations of $\sim 14^\circ$ between D1 and D2 domains within a given protomer (Fig. S5). To validate the asymmetrical split-ring structure, we used a combined biochemical and solution NMR approach. We show that a single interprotomer disulfide bond connecting protomers 1 and 6 can be formed between cysteine residues introduced at positions 111 (NTD) and 494 (D2). This cross-link is consistent with the cryo-EM model of the split-ring conformation, which places residues 111 of protomer 6 and 494 of protomer 1 within 8 Å of each other, whereas the remaining cysteine–cysteine distances in the split-ring form and all such distances in the stacked-ring conformation are greater than 43 Å. Further, cryo-EM studies of the disulfide-linked complex in the ATP-loaded state establish that only the split-ring structure is formed, in contrast to the mixed population of split- and stacked-ring structures present in wt VAT under similar conditions.

Additional validation experiments were done using methyl-TROSY-based solution NMR. Here, we used an approach whereby a single NMR methyl probe is added at a key site that has been converted to a cysteine residue in a highly deuterated protein to form $^{13}\text{CH}_3$ -labeled S-methylthio-cysteine (46). There is no need for assignment of the observed resonance (or resonances) because it (or they) must derive from the added probe, so that NMR studies can proceed rapidly. Methyl probes attached at either D2 domain position 652 or 684 establish a pair of unique states, A and B, that report on protomers 6 (and possibly 5) and 1–4, respectively. Paramagnetic relaxation enhancement experiments of ADP-VAT using the water-soluble reagent Gd(III)DTPA-BMA show that state A is much more surface-exposed, as expected from the cryo-EM structure of ADP-VAT, and that local dynamics of the methyl probe at position 684 are much larger in state A than in state B. NMR magnetization exchange experiments further establish that an upper bound for the rate of interconversion between states A and B is 0.2 s^{-1} (Fig. S8), which is in keeping with the large conformational changes that are required. It is worth emphasizing that the $^{13}\text{CH}_3$ -labeled S-methylthio-cysteines at positions 652 and 684 are unlikely to perturb the structure because the original residues at these positions were methionines with the only difference between S-methylthiocysteine and methionine being the replacement of C γ by S.

NMR spectra of M684C- $^{13}\text{CH}_3$ VAT were recorded in apo, ADP, and ATP γ S states, showing that nucleotides shift the relative intensities of peaks A and B from $\sim 10:90$ (ATP γ S) to $30:70$ (ADP), with a ratio of $20:80$ for apo-VAT (as measured by peak integration). From these data, and assuming that ADP-VAT forms only the split-ring conformer in solution, as observed in cryo-EM specimens, a $28:72$ ratio between split- and stacked-ring structures is calculated for the ATP γ S-loaded form of the enzyme. This result is in reasonable agreement with the $42 \pm 2:58 \pm 2$ ratio estimated from image classification of conformers in EM specimens obtained with two different starting models (Fig. 5B and Fig. S9), and suggests that rapid freezing during the process of sample preparation for cryo-EM analysis largely preserves the equilibrium solution distribution of VAT conformers. Differences in ratios may reflect the fact that VAT is frozen from 4°C , whereas NMR spectra were recorded at 60°C . It is worth noting that the populations of the VAT conformers were of similar magnitude in the present study. It will be of interest to do further comparisons between cryo-EM and NMR-based measurements, focusing on systems where it is known from NMR studies that the relative populations are more highly skewed, keeping in mind that temperature differences can change expected distributions of conformers.

The sixfold symmetrical, stacked-ring conformation of ATP γ S-loaded VAT resembles the crystal structure of homologous *Mus musculus* p97/VCP in complex with a mixture of ADP and ADP-AIF $_6$ (42) and recent high-resolution cryo-EM structures of p97 in different nucleotide states (38, 39) and in the presence or absence of an allosteric inhibitor (38). Consequently, it was surprising to observe that in the ADP-bound conformation, the protomers arrange in a helical manner so as to generate an asymmetrical, split-ring structure. That a similar conformer has not been observed for p97, especially considering the high degree of sequence identity between the two molecules (55% when the NTD is excluded), may well reflect distinct functional mechanisms for p97 and VAT. For example, biochemical and structural studies suggest that p97 likely does not function by unfolding substrates and passing them through its central pore (42, 59) and a key Tyr-Tyr sequence in the pore loops of VAT D1 that is implicated in substrate translocation is replaced by Leu-Ala in p97 (23).

Notably, there are precedents for asymmetrical AAA+ ATPase rings, as observed for ADP-VAT. For example, ClpX, a prokaryotic unfoldase consisting of a single AAA+ ring, forms a highly asymmetrical structure that is closely correlated to its mechanism of nucleotide binding and hydrolysis as well as substrate unfolding (2). A related asymmetrical structure was also recently observed for Vps4, a single AAA+ ring involved in membrane remodeling (4). NSF, an AAA+ protein closely related to VAT and p97/VCP/Cdc48, is also composed of tandem ATPase rings. A recent cryo-EM study reported a “washer-shaped” AAA+ ring structure for the D1 domains of NSF, with an “open,” essentially planar ring structure observed in the ADP-bound state and a “closed” structure for the ATP conformation, whereby each D1 domain is translated by ~ 5 Å along the axis extending from D1 to D2 (60).

The helical architecture of VAT in the ADP-bound state is somewhat reminiscent of the structure of the single-ring AAA+ unfoldase component of the 19S regulatory particle from the 26S proteasome, where Rpt1–6 subunits are also arranged in a spiral-staircase manner (9, 10). This type of helical arrangement is often observed for other AAA+ proteins, such as the yeast replication factor C (61), the bacterial DnaA AAA+ domain (62), the bacterial IstB domain (63), and the eukaryotic MCM E1 helicase (64), implying a potential evolutionary conservation in the architecture of these proteins despite varying structural features and distinct biological functions.

It has been proposed that VAT functions via a substrate threading mechanism (18) similar to the mechanism used by other AAA+ unfoldases, such as ClpX and ClpA (65, 66), whereby protein substrates are unfolded and threaded through the central pore of the unfoldase and subsequently passed into the degradation chamber of the 20S proteasome CP. The mechanical force for this process is generated from repeated cycles of ATP binding and hydrolysis. Substrates are pulled through the narrow channel of the unfoldase via attachment to pore loops located at the entrance and in the interior of the channel (65, 67–70), which also play a role in substrate recognition in some AAA+ machines (5, 71–73). In the case of VAT, mutations of pore loop residues Y264 in D1 and W541/V542 in D2 cause severe defects on substrate unfolding and translocation (18). The stacked- and split-ring structures reported here suggest a plausible model for the substrate unfolding mechanism of VAT that is coupled to ATP hydrolysis (Fig. 7). In the stacked-ring, symmetrical conformation of ATP-VAT, the pore loops in D1 localize to the entrance of the central channel in a coplanar fashion and provide the point of initial contact with substrate at the beginning of the ATP hydrolysis cycle. ATP hydrolysis leads to a conformational change, placing the pore loops at different *z* positions in the split-ring conformer so as to generate differential pulling forces on various parts of the substrate. The central pore of the stacked-ring conformation is disrupted in the split-ring conformation to become a helix. The path through the complex enclosed by this helical opening is constricted relative to the pore of the stacked-ring, as seen in [Movie S1](#). The net result is an unraveling of structure and concomitant translocation into the degradation machinery (Fig. 7). In addition, the structural rearrangements that accompany ATP hydrolysis would destroy the pair of nucleotide binding sites on the interface between protomers 1 and 6, possibly promoting ADP release at the end of the reaction cycle so that ATP can be reloaded for the next round of hydrolysis.

The structural asymmetry and the large conformational changes that accompany nucleotide binding and hydrolysis, as described here in the context of VAT, are also features of other AAA+-based molecular machines. Such structural changes likely

play important roles in generating the mechanical forces that are necessary to act on the target substrates, although the details will vary with each system. It is clear that recent developments in both cryo-EM and solution NMR now set the stage for in-depth studies of how changes in molecular conformation in a variety of different supramolecular assemblies translate into function.

Materials and Methods

EM. Purified VAT at 7 mg/mL in buffer [50 mM Hepes, 100 mM NaCl (pH 7.5)] was incubated with 5 mM nucleotide, ADP, or ATPγS (Sigma–Aldrich) for 5 min at room temperature before freezing. Immediately before freezing, 0.05% (wt/vol) IGEPAL CA-630 (Sigma–Aldrich) was added to the purified VAT to increase the number of particles adopting side views on the EM grid. A total of 2.5 μL of sample was applied onto nanofabricated holey carbon grids (74) with a hole size of ~1 μm and blotted using a modified FEI Vitrobot for 5 s before plunge-freezing in a liquid ethane/propane mixture (ratio of ~60:40%). VAT* was prepared for imaging in the same way as wt VAT, but with ATP instead of ATPγS to prevent reduction of the disulfide bond. Movies consisting of 30 frames with two frames per second were collected with defocuses ranging from 1.8 to 3.5 μm using a FEI Tecnai F20 microscope operating at 200 kV and equipped with a Gatan K2 DDD camera. Movies were collected in counting mode with an exposure of five electrons per pixel per second, with a total exposure of ~35 electrons per square angstrom. Additional details are provided in [SI Materials and Methods](#).

NMR Experiments. All NMR experiments were performed on Varian Inova and Bruker Avance III HD 14.0-T spectrometers equipped with cryogenically cooled, pulse-field gradient triple-resonance probes. The ¹³C-¹H HMQC spectra were recorded at 60 °C, exploiting a methyl-TROSY effect to obtain high-quality datasets (35). Sample (subunit) concentrations varied from 500 to 800 μM, with protein dissolved in the NMR buffer [25 mM potassium phosphate, 50 mM NaCl, 4.3 mM NaN₃, 1 mM EDTA (pH 7.5) in 99.9% D₂O]. Nucleotides (ADP or ATPγS) were added into the NMR sample to a final concentration of 5 mM. For ATPγS-bound VAT, 10 mM MgCl₂ was also included in the buffer.

A description of protein expression and purification, further details of NMR experiments, and a discussion of functional assays are given in [SI Materials and Methods](#).

ACKNOWLEDGMENTS. We thank Prof. Arthur Horwich (Yale University) for kindly providing the GroEL construct used in activity assays. This work was supported through grants from the Canadian Institutes of Health Research (to L.E.K. and J.L.R.). L.E.K. and J.L.R. hold Canada Research Chairs.

- Hanson PI, Whiteheart SW (2005) AAA+ proteins: Have engine, will work. *Nat Rev Mol Cell Biol* 6(7):519–529.
- Glynn SE, Martin A, Nager AR, Baker TA, Sauer RT (2009) Structures of asymmetric ClpX hexamers reveal nucleotide-dependent motions in a AAA+ protein-unfolding machine. *Cell* 139(4):744–756.
- Bochtler M, et al. (2000) The structures of HslU and the ATP-dependent protease HslU-HslV. *Nature* 403(6771):800–805.
- Caillat C, et al. (2015) Asymmetric ring structure of Vps4 required for ESCRT-III disassembly. *Nat Commun* 6:8781.
- Weibezahn J, et al. (2004) Thermotolerance requires refolding of aggregated proteins by substrate translocation through the central pore of ClpB. *Cell* 119(5):653–665.
- Parsell DA, Kowal AS, Singer MA, Lindquist S (1994) Protein disaggregation mediated by heat-shock protein Hsp104. *Nature* 372(6505):475–478.
- Sauer RT, Baker TA (2011) AAA+ proteases: ATP-fueled machines of protein destruction. *Annu Rev Biochem* 80:587–612.
- Goldberg AL (2003) Protein degradation and protection against misfolded or damaged proteins. *Nature* 426(6968):895–899.
- Beckwith R, Estrin E, Worden EJ, Martin A (2013) Reconstitution of the 26S proteasome reveals functional asymmetries in its AAA+ unfoldase. *Nat Struct Mol Biol* 20(10):1164–1172.
- Lander GC, et al. (2012) Complete subunit architecture of the proteasome regulatory particle. *Nature* 482(7384):186–191.
- Unverdorben P, et al. (2014) Deep classification of a large cryo-EM dataset defines the conformational landscape of the 26S proteasome. *Proc Natl Acad Sci USA* 111(15):5544–5549.
- Chamieh H, Guetta D, Franzetti B (2008) The two PAN ATPases from Halobacterium display N-terminal heterogeneity and form labile complexes with the 20S proteasome. *Biochem J* 411(2):387–397.
- Smith DM, Fraga H, Reis C, Kafri G, Goldberg AL (2011) ATP binds to proteasomal ATPases in pairs with distinct functional effects, implying an ordered reaction cycle. *Cell* 144(4):526–538.
- Wilson HL, Ou MS, Aldrich HC, Maupin-Furlow J (2000) Biochemical and physical properties of the Methanococcus jannaschii 20S proteasome and PAN, a homolog of the ATPase (Rpt) subunits of the eucaryal 26S proteasome. *J Bacteriol* 182(6):1680–1692.
- Wang T, et al. (2009) Structural insights on the Mycobacterium tuberculosis proteasomal ATPase Mpa. *Structure* 17(10):1377–1385.
- Pamnani V, et al. (1997) Cloning, sequencing and expression of VAT, a CDC48/p97 ATPase homologue from the archaeon Thermoplasma acidophilum. *FEBS Lett* 404(2–3):263–268.
- Rockel B, Jakana J, Chiu W, Baumeister W (2002) Electron cryo-microscopy of VAT, the archaeal p97/CDC48 homologue from Thermoplasma acidophilum. *J Mol Biol* 317(5):673–681.
- Gerega A, et al. (2005) VAT, the thermoplasma homolog of mammalian p97/VCP, is an N domain-regulated protein unfoldase. *J Biol Chem* 280(52):42856–42862.
- Barthelme D, Sauer RT (2012) Identification of the Cdc48•20S proteasome as an ancient AAA+ proteolytic machine. *Science* 337(6096):843–846.
- Barthelme D, Sauer RT (2013) Bipartite determinants mediate an evolutionarily conserved interaction between Cdc48 and the 20S peptidase. *Proc Natl Acad Sci USA* 110(9):3327–3332.
- Forouzand D, et al. (2012) The archaeal proteasome is regulated by a network of AAA ATPases. *J Biol Chem* 287(46):39254–39262.
- Vij N (2008) AAA ATPase p97/VCP: Cellular functions, disease and therapeutic potential. *J Cell Mol Med* 12(6A):2511–2518.
- Rothballer A, Tzvetkov N, Zwickl P (2007) Mutations in p97/VCP induce unfolding activity. *FEBS Lett* 581(6):1197–1201.
- Wendler P, Ciniawsky S, Kock M, Kube S (2012) Structure and function of the AAA+ nucleotide binding pocket. *Biochim Biophys Acta* 1823(1):2–14.
- Bar-Nun S, Glickman MH (2012) Proteasomal AAA-ATPases: Structure and function. *Biochim Biophys Acta* 1823(1):67–82.
- Erzberger JP, Berger JM (2006) Evolutionary relationships and structural mechanisms of AAA+ proteins. *Annu Rev Biophys Biomol Struct* 35(1):93–114.
- Kühlbrandt W (2014) Biochemistry. The resolution revolution. *Science* 343(6178):1443–1444.
- Smith MTJ, Rubinstein JL (2014) Structural biology. Beyond blob-ology. *Science* 345(6197):617–619.

29. Fiaux J, Bertelsen EB, Horwich AL, Wüthrich K (2002) NMR analysis of a 900K GroEL GroES complex. *Nature* 418(6894):207–211.
30. Sprangers R, Kay LE (2007) Quantitative dynamics and binding studies of the 20S proteasome by NMR. *Nature* 445(7128):618–622.
31. Bai XC, et al. (2015) An atomic structure of human γ -secretase. *Nature* 525(7568):212–217.
32. Zhao J, Benlekkir S, Rubinstein JL (2015) Electron cryomicroscopy observation of rotational states in a eukaryotic V-ATPase. *Nature* 521(7551):241–245.
33. Llácer JL, et al. (2015) Conformational Differences between Open and Closed States of the Eukaryotic Translation Initiation Complex. *Mol Cell* 59(3):399–412.
34. Pervushin K, Riek R, Wider G, Wüthrich K (1997) Attenuated T2 relaxation by mutual cancellation of dipole-dipole coupling and chemical shift anisotropy indicates an avenue to NMR structures of very large biological macromolecules in solution. *Proc Natl Acad Sci USA* 94(23):12366–12371.
35. Tugarinov V, Hwang PM, Ollerenshaw JE, Kay LE (2003) Cross-correlated relaxation enhanced ¹H[¹³C] NMR spectroscopy of methyl groups in very high molecular weight proteins and protein complexes. *J Am Chem Soc* 125(34):10420–10428.
36. Tugarinov V, Kay LE (2004) An isotope labeling strategy for methyl TROSY spectroscopy. *J Biomol NMR* 28(2):165–172.
37. Rosenzweig R, Kay LE (2016) Solution NMR Spectroscopy Provides an Avenue for the Study of Functionally Dynamic Molecular Machines: The Example of Protein Disaggregation. *J Am Chem Soc* 138(5):1466–1477.
38. Banerjee S, et al. (2016) 2.3 Å resolution cryo-EM structure of human p97 and mechanism of allosteric inhibition. *Science* 351(6275):871–875.
39. Schuller JM, Beck F, Lössl P, Heck AJR, Förster F (2016) Nucleotide-dependent conformational changes of the AAA+ ATPase p97 revisited. *FEBS Lett* 590(5):595–604.
40. Davies JM, Brunger AT, Weiss WI (2008) Improved structures of full-length p97, an AAA ATPase: Implications for mechanisms of nucleotide-dependent conformational change. *Structure* 16(5):715–726.
41. Huyton T, et al. (2003) The crystal structure of murine p97/VCP at 3.6 Å. *J Struct Biol* 144(3):337–348.
42. DeLaBarre B, Brunger AT (2003) Complete structure of p97/valosin-containing protein reveals communication between nucleotide domains. *Nat Struct Biol* 10(10):856–863.
43. Trabuco LG, Villa E, Mitra K, Frank J, Schulten K (2008) Flexible fitting of atomic structures into electron microscopy maps using molecular dynamics. *Structure* 16(5):673–683.
44. Barthelme D, Chen JZ, Grabenstatter J, Baker TA, Sauer RT (2014) Architecture and assembly of the archaeal Cdc48*20S proteasome. *Proc Natl Acad Sci USA* 111(17):E1687–E1694.
45. Kucukelbir A, Sigworth FJ, Tagare HD (2014) Quantifying the local resolution of cryo-EM density maps. *Nat Methods* 11(1):63–65.
46. Religa TL, Ruschak AM, Rosenzweig R, Kay LE (2011) Site-directed methyl group labeling as an NMR probe of structure and dynamics in supramolecular protein systems: Applications to the proteasome and to the ClpP protease. *J Am Chem Soc* 133(23):9063–9068.
47. Choy WY, et al. (2002) Distribution of molecular size within an unfolded state ensemble using small-angle X-ray scattering and pulse field gradient NMR techniques. *J Mol Biol* 316(1):101–112.
48. Bernini A, et al. (2008) NMR studies on the surface accessibility of the archaeal protein Sso7d by using TEMPOL and Gd(III)(DTPA-BMA) as paramagnetic probes. *Biophys Chem* 137(2-3):71–75.
49. Tugarinov V, Kay LE (2006) Relaxation rates of degenerate ¹H transitions in methyl groups of proteins as reporters of side-chain dynamics. *J Am Chem Soc* 128(22):7299–7308.
50. Kontaxis G, Bax A (2001) Multiplet component separation for measurement of methyl ¹³C-¹H dipolar couplings in weakly aligned proteins. *J Biomol NMR* 20(1):77–82.
51. Werbelow LG, Grant DM (1977) Intramolecular dipolar relaxation in multispin systems. *Adv Magn Opt Reson* 9:189–299.
52. Kay LE, Torchia D (1991) The effects of dipolar cross correlation on ¹³C methyl-carbon T1, T2, and NOE measurements in macromolecules. *J Magn Reson* 95(3):536–547.
53. Farrow NA, Zhang O, Forman-Kay JD, Kay LE (1994) A heteronuclear correlation experiment for simultaneous determination of ¹⁵N longitudinal decay and chemical exchange rates of systems in slow equilibrium. *J Biomol NMR* 4(5):727–734.
54. Scheres SHW, et al. (2007) Disentangling conformational states of macromolecules in 3D-EM through likelihood optimization. *Nat Methods* 4(1):27–29.
55. Scheres SHW (2012) RELION: Implementation of a Bayesian approach to cryo-EM structure determination. *J Struct Biol* 180(3):519–530.
56. Weber-Ban EU, Reid BG, Miranker AD, Horwich AL (1999) Global unfolding of a substrate protein by the Hsp100 chaperone ClpA. *Nature* 401(6748):90–93.
57. Rosenzweig R, Kay LE (2014) Bringing dynamic molecular machines into focus by methyl-TROSY NMR. *Annu Rev Biochem* 83:291–315.
58. Sekhar A, Kay LE (2013) NMR paves the way for atomic level descriptions of sparsely populated, transiently formed biomolecular conformers. *Proc Natl Acad Sci USA* 110(32):12867–12874.
59. DeLaBarre B, Christianson JC, Kopito RR, Brunger AT (2006) Central pore residues mediate the p97/VCP activity required for ERAD. *Mol Cell* 22(4):451–462.
60. Zhao M, et al. (2015) Mechanistic insights into the recycling machine of the SNARE complex. *Nature* 518(7537):61–67.
61. Bowman GD, O'Donnell M, Kuriyan J (2004) Structural analysis of a eukaryotic sliding DNA clamp-clamp loader complex. *Nature* 429(6993):724–730.
62. Erzberger JP, Mott ML, Berger JM (2006) Structural basis for ATP-dependent DnaA assembly and replication-origin remodeling. *Nat Struct Mol Biol* 13(8):676–683.
63. Arias-Palomo E, Berger JM (2015) An Atypical AAA+ ATPase Assembly Controls Efficient Transposition through DNA Remodeling and Transposase Recruitment. *Cell* 162(4):860–871.
64. Enemark EJ, Joshua-Tor L (2006) Mechanism of DNA translocation in a replicative hexameric helicase. *Nature* 442(7100):270–275.
65. Olivares AO, Nager AR, Iosefson O, Sauer RT, Baker TA (2014) Mechanochemical basis of protein degradation by a double-ring AAA+ machine. *Nat Struct Mol Biol* 21(10):871–875.
66. Cordova JC, et al. (2014) Stochastic but highly coordinated protein unfolding and translocation by the ClpXP proteolytic machine. *Cell* 158(3):647–658.
67. Yamada-Inagawa T, Okuno T, Karata K, Yamanaka K, Ogura T (2003) Conserved pore residues in the AAA protease FtsH are important for proteolysis and its coupling to ATP hydrolysis. *J Biol Chem* 278(50):50182–50187.
68. Iosefson O, Nager AR, Baker TA, Sauer RT (2015) Coordinated gripping of substrate by subunits of a AAA+ proteolytic machine. *Nat Chem Biol* 11(3):201–206.
69. Iosefson O, Olivares AO, Baker TA, Sauer RT (2015) Dissection of Axial-Pore Loop Function during Unfolding and Translocation by a AAA+ Proteolytic Machine. *Cell Reports* 12(6):1032–1041.
70. Martin A, Baker TA, Sauer RT (2008) Pore loops of the AAA+ ClpX machine grip substrates to drive translocation and unfolding. *Nat Struct Mol Biol* 15(11):1147–1151.
71. Siddiqui SM, Sauer RT, Baker TA (2004) Role of the processing pore of the ClpX AAA+ ATPase in the recognition and engagement of specific protein substrates. *Genes Dev* 18(4):369–374.
72. Flynn JM, et al. (2001) Overlapping recognition determinants within the ssrA degradation tag allow modulation of proteolysis. *Proc Natl Acad Sci USA* 98(19):10584–10589.
73. Schlieker C, et al. (2004) Substrate recognition by the AAA+ chaperone ClpB. *Nat Struct Mol Biol* 11(7):607–615.
74. Marr CR, Benlekkir S, Rubinstein JL (2014) Fabrication of carbon films with ~ 500nm holes for cryo-EM with a direct detector device. *J Struct Biol* 185(1):42–47.
75. Bouvignies G, et al. (2011) Solution structure of a minor and transiently formed state of a T4 lysozyme mutant. *Nature* 477(7362):111–114.
76. Delaglio F, et al. (1995) NMRPipe: A multidimensional spectral processing system based on UNIX pipes. *J Biomol NMR* 6(3):277–293.
77. Goddard TD, Kneller DG (2008) SPARKY 3 (University of California, San Francisco).
78. Rubinstein JL, Brubaker MA (2015) Alignment of cryo-EM movies of individual particles by optimization of image translations. *J Struct Biol* 192(2):188–195.
79. Rohou A, Grigorieff N (2015) CTFIND4: Fast and accurate defocus estimation from electron micrographs. *J Struct Biol* 192(2):216–221.
80. Scheres SHW (2015) Semi-automated selection of cryo-EM particles in RELION-1.3. *J Struct Biol* 189(2):114–122.
81. Zhao J, Brubaker MA, Benlekkir S, Rubinstein JL (2015) Description and comparison of algorithms for correcting anisotropic magnification in cryo-EM images. *J Struct Biol* 192(2):209–215.
82. Yeung HO, et al. (2014) Inter-ring rotations of AAA ATPase p97 revealed by electron cryomicroscopy. *Open Biol* 4:130142.
83. Altschul SF, et al. (1997) Gapped BLAST and PSI-BLAST: A new generation of protein database search programs. *Nucleic Acids Res* 25(17):3389–3402.
84. Li W, Godzik A (2006) Cd-hit: A fast program for clustering and comparing large sets of protein or nucleotide sequences. *Bioinformatics* 22(13):1658–1659.
85. Pei J, Sadreyev R, Grishin NV (2003) PCMA: Fast and accurate multiple sequence alignment based on profile consistency. *Bioinformatics* 19(3):427–428.
86. McGuffin LJ, Bryson K, Jones DT (2000) The PSIPRED protein structure prediction server. *Bioinformatics* 16(4):404–405.
87. Kuroski MA, Bujnicki JM (2003) GeneSilico protein structure prediction meta-server. *Nucleic Acids Res* 31(13):3305–3307.
88. Ginals K, Rychlewski L (2003) Protein structure prediction of CASP5 comparative modeling and fold recognition targets using consensus alignment approach and 3D assessment. *Proteins* 53(Suppl 6):410–417.
89. Jaroszewski L, Li Z, Cai XH, Weber C, Godzik A (2011) FFAS server: Novel features and applications. *Nucleic Acids Res* 39(Web Server issue, Suppl 2):W38–W44.
90. Söding J (2005) Protein homology detection by HMM-HMM comparison. *Bioinformatics* 21(7):951–960.
91. Fiser A, Sali A (2003) Modeller: Generation and refinement of homology-based protein structure models. *Methods Enzymol* 374:461–491.
92. Wiederstein M, Sippl MJ (2007) ProSA-web: Interactive web service for the recognition of errors in three-dimensional structures of proteins. *Nucleic Acids Res* 35(Web Server issue, Suppl 2):W407–W410.
93. Goddard TD, Huang CC, Ferrin TE (2007) Visualizing density maps with UCSF Chimera. *J Struct Biol* 157(1):281–287.
94. Pintilie GD, Zhang J, Goddard TD, Chiu W, Gossard DC (2010) Quantitative analysis of cryo-EM density map segmentation by watershed and scale-space filtering, and fitting of structures by alignment to regions. *J Struct Biol* 170(3):427–438.
95. Nørby JG (1988) Coupled assay of Na⁺,K⁺-ATPase activity. *Methods Enzymol* 156:116–119.
96. Rosenzweig R, Moradi S, Zarrine-Afsar A, Glover JR, Kay LE (2013) Unraveling the mechanism of protein disaggregation through a ClpB-DnaK interaction. *Science* 339(6123):1080–1083.
97. McConnell HM (1958) Reaction rates by nuclear magnetic resonance. *J Chem Phys* 28(3):430–431.